

## 1 Red wood-ant nests are traps for fault-related CH<sub>4</sub> micro-seepage

2 G.M. Berberich<sup>1</sup>, A.M. Ellison<sup>2</sup>, J. Hartmann<sup>3</sup>, M.B. Berberich<sup>4</sup>, A. Grumpe<sup>1</sup>, A. Becker<sup>1</sup>, C. Wöhler<sup>1</sup>

3 <sup>1</sup>Technical University of Dortmund, Faculty of Electrical Engineering and Information Technology,  
4 Image Analysis Group, Otto-Hahn-Straße 4, 44227 Dortmund, Germany; **Corresponding author:**  
5 [gabriele.berberich@tu-dortmund.de](mailto:gabriele.berberich@tu-dortmund.de); Tel: +49-231-755-4518 or +49-2235-955233

6 <sup>2</sup>Harvard University, Harvard Forest, 324 North Main Street, Petersham, Massachusetts, 01366 USA

7 <sup>3</sup>Institut für Geowissenschaften, Universität Heidelberg, Im Neuenheimer Feld 236, 69120 Heidelberg

8 <sup>4</sup>IT-Consulting Berberich, Am Plexer 7, 50374 Erftstadt, Germany

## 9 Abstract

10 Methane (CH<sub>4</sub>) is common on Earth, forms the major commercial natural gas reservoirs, and is a key  
11 component of the global carbon cycle, but its natural sources are not well-characterized. We present a  
12 geochemical dataset acquired from a red wood-ant (RWA; *Formica polyctena*) nest in the Neuwied  
13 Basin, a part of the East Eifel Volcanic Field (EEVF), focusing on methane (CH<sub>4</sub>), stable carbon isotope  
14 of methane ( $\delta^{13}\text{C-CH}_4$ ), RWA activity patterns, earthquakes, and earth tides. Nest gas and ambient air  
15 were analyzed to detect microbial, thermogenic, and abiotic fault-related micro-seepage. Neither  
16 methane degassing nor RWA activity was synchronized with earth tides. Two  $\delta^{13}\text{C-CH}_4$  signatures were  
17 identified in nest gas: -69‰ and -37‰. The -69‰ signature of  $\delta^{13}\text{C-CH}_4$  within the RWA nest is attributed  
18 to microbial decomposition of organic matter. This finding supports previous findings that RWA nests  
19 are hot-spots of microbial CH<sub>4</sub>. Additionally, the -37‰  $\delta^{13}\text{C-CH}_4$  signature is the first evidence that RWA  
20 nests also serve as traps for fault-related emissions of CH<sub>4</sub>. The -37‰  $\delta^{13}\text{C-CH}_4$  signature can be  
21 attributed either to thermogenic/fault-related or to abiotic/fault-related CH<sub>4</sub> formation originating from  
22 e.g. low-temperature gas-water-rock reactions in a continental setting at shallow depths (micro-  
23 seepage). Sources of these micro-seeps could be Devonian schists (“Sphaerosiderith Schiefer”) with  
24 iron concretions (“Eisengallen”), sandstones, or the iron-bearing “Klerf Schichten”. We cannot exclude  
25 overlapping micro-seepage of magmatic CH<sub>4</sub> from the Eifel plume. Given the abundance of RWA nests  
26 on the landscape, their role as sources of microbial CH<sub>4</sub> and traps for abiotically-derived CH<sub>4</sub> should be  
27 included in estimation of methane emissions that are contributing to climatic change.

28 **Keywords**

29 red wood ants, *Formica polyctena*, CH<sub>4</sub>, δ<sup>13</sup>C-CH<sub>4</sub>, fault, activity pattern

30 **Acknowledgements**

31 We thank Daniela Polag (University of Heidelberg) for doing the nest-gas sampling and analyses. RWA  
32 activity recording was done using equipment from the Department of Geology at University of Duisburg-  
33 Essen. We also thank Dr. Peter Henrich (Leiter der Direktion Landesarchäologie - Außenstelle Koblenz)  
34 for his permission to conduct the survey on the Goloring site, and Hans-Toni Dickers, Paul Görger and  
35 Bernd Klug from Kuratorium für Heimatforschung und -pflege, Koblenz-Gondorf for their support during  
36 the field campaign.

37 **Funding**

38 The study is part of the research project “GeoBio-Interactions” funded by the VW-Stiftung (Az 93 403).

39

## 40 1 Introduction

41 Methane (CH<sub>4</sub>) is common on Earth, forms the major commercial natural gas reservoirs, and is a key  
42 component of the global carbon cycle (Keppler et al 2009; Etiope and Sherwood Lollar 2013). This  
43 second-most important greenhouse gas currently has an average atmospheric concentration of 1.82  
44 ppm, and continues to increase (Saunio et al. 2016). Today, most natural occurrences of CH<sub>4</sub> are  
45 associated with terrestrial and aquatic processes. In the shallow subsurface, CH<sub>4</sub> is produced on  
46 geological time scales mainly by thermal conversion of organic matter resulting from heat and pressure  
47 deep in the Earth's crust or by microbial activity. This biotic CH<sub>4</sub> includes the formation of thermogenic  
48 CH<sub>4</sub> and microbial acetoclastic methanogenesis (Etiope and Schoell 2014; Kiätävienien and Purkamo  
49 2015). In contrast, abiotic CH<sub>4</sub> is produced in much smaller amounts on a global scale and is formed by  
50 either high-temperature magmatic processes (Sabatier-type reactions) in volcanic and geothermal  
51 areas, or via low-temperature (<100 °C) Fischer-Tropsch-Type (FTT) gas-water-rock reactions in  
52 continental settings, even at shallow depths. It is found in specific geologic environments, including  
53 volcanic and geothermal systems; fluid inclusions in igneous intrusions; crystalline rocks in Precambrian  
54 Shields; and submarine, serpentinite-hosted hydrothermal fields or land-based serpentinization fluids  
55 (Etiope and Sherwood Lollar 2013; Etiope and Schoell 2014).

56 In most geologic environments, biotic and abiotic gases occur simultaneously. Both thermogenic and  
57 abiotic CH<sub>4</sub> reach the atmosphere through marine and terrestrial geologic gas (micro-)seeps, and during  
58 the exploitation and distribution of fossil fuels. To identify whether locally elevated CH<sub>4</sub> concentrations  
59 in the atmosphere are due transportation via fault networks, a determination of possible methane  
60 source(s) is required. At the land surface, CH<sub>4</sub> is produced by methanogenic Archaea in anaerobic soil  
61 environments or through oxidation by methanotrophic bacteria in aerobic topsoils (Jílková et al. 2016).  
62 Isotopic measurements of δ<sup>13</sup>C-CH<sub>4</sub> can distinguish abiotic from biotic CH<sub>4</sub> (Schoell 1980; Keppler et al.  
63 2006).

64 Increase in compressive stress, changes in the volume of the pore fluid or rock matrix, and fluid  
65 movement or buoyancy are important mechanisms driving fluid flow and keeping fractures open (Birdsell  
66 et al. 2015; Boothroyd et al. 2016). Faults and fracture networks act as preferential pathways of lateral  
67 and vertical degassing, creating linear fault-linked anomalies, irregularly-shaped diffuse or "halo"  
68 anomalies and irregularly-spaced plumes or "spot anomalies" (e.g. Ciotoli et al. 2006; Etiope 2009).  
69 Boothroyd et al. (2016) showed that faults had δ<sup>13</sup>C-CH<sub>4</sub> = -37‰ and a significantly higher CH<sub>4</sub> flux

70 (11.5±6.3 t CH<sub>4</sub> km<sup>-1</sup> yr<sup>-1</sup>) than control zones. In Europe, micro-seeps occur both onshore and offshore,  
71 with estimated CH<sub>4</sub> flux in Europe of 0.8 Tg yr<sup>-1</sup> and total seepage of 3 Tg yr<sup>-1</sup> (Etioppe 2009, Kietäväinen  
72 and Purkamo 2015).

73 Recent research has revealed close relationships between the spatial distribution of red wood-ant nests  
74 (*Formica rufa*-group; henceforth RWA) and tectonic fault zones (Berberich 2010; Berberich and  
75 Schreiber 2013; Berberich et al. 2016; del Toro et al. 2017). Exploratory testing of fault-zone gases  
76 revealed that helium (He) and radon (Rn) in RWA nests exceeded atmospheric and background  
77 concentrations (Berberich 2010; Berberich and Schreiber 2013; Berberich et al. 2016). However, little  
78 consideration has been given to the natural release of CH<sub>4</sub> from RWA nests (Jílková et al. 2016) or via  
79 fault zones (Boothroyd et al. 2016), although there are a range of processes that could contribute to it,  
80 including micro-seepage via buoyant flux of CH<sub>4</sub>, faults increasing the flow rate of microbubbles, and  
81 gas vents or response to earth tides and earthquakes (Crockett et al. 2010; Etioppe and Klusman 2002).

82 We used a combination of geochemical, geophysical, and biological techniques; state-of-the-art image  
83 analysis; and statistical methods to identify associations between RWA activity, CH<sub>4</sub> degassing, earth  
84 tides, and tectonic processes. We explored whether RWA nests are associated with actively degassing  
85 faults or traps for migrating CH<sub>4</sub> from the deep underground, and if RWA activity changed during the  
86 (micro)-seepage process. Specifically, we tested the null hypotheses that, in the field, RWA activity and  
87 concentrations of both CH<sub>4</sub> and δ<sup>13</sup>C-CH<sub>4</sub> are independent.

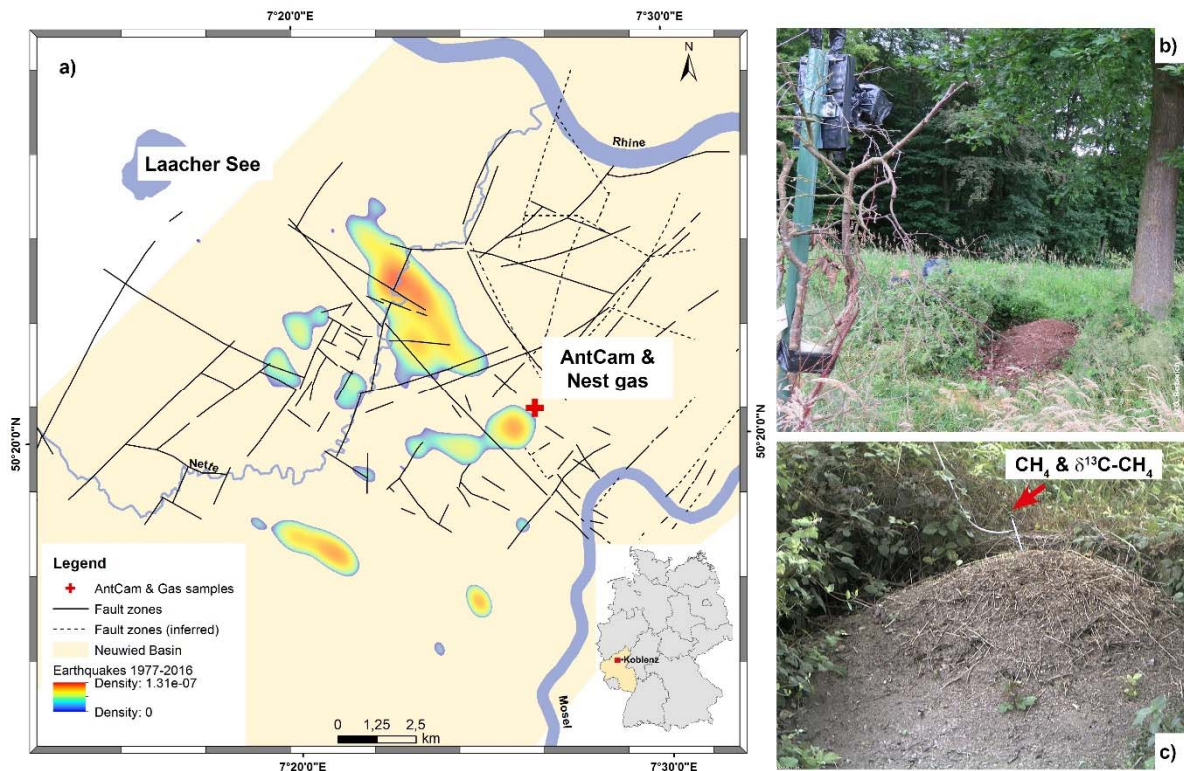
## 88 **2 Methods**

89 We explored associations between RWA activity, methane concentrations in ant nests and ambient  
90 air, tectonic events, weather processes, and earth tides at the Goloring site near Koblenz, Germany  
91 during an 8-d sampling campaign that ran from 4–11 August 2016.

### 92 **2.1 Study area**

93 The Goloring site is located west of the Rhine River, southeast of the Laacher See volcano, and close  
94 to the Ochtendung Fault Zone in the seismically active Neuwied Basin, which is part of the Quaternary  
95 East Eifel Volcanic field (EEVF; western Germany; Fig. 1a). The EEVF includes ≈100 Quaternary  
96 volcanic eruption centers; the Laacher See volcano experienced a phreato-plinian eruption ≈12,900  
97 years ago (Litt et al. 2001). The Paleozoic basement consists of alternating strata of Devonian, iron-

98 bearing, quartzitic sandstones with a carbonate matrix and argillaceous shale reaching to 5-km depths.  
99 Several thin black coal seams (Upper Siegen) are embedded within these alternating strata (LGB RLP  
100 2005). Eocene/Oligocene lignite seams are found at  $\approx 75\text{--}160$  m and are covered by Paleogene  
101 volcanites and Neogene clastic sediments. The study area has been affected by complex major tectonic  
102 and magmatic processes, including plume-related thermal expansion of the mantle-lithosphere (Ritter  
103 et al. 2001; Walker et al. 2005; Tesauro et al. 2006), crustal thinning and associated volcanism (Clauser  
104 2002), active rifting processes (Hinzen 2003), and possibly crustal-scale folding or the reactivation of  
105 Variscan thrust faults under the present-day NW–SE-directed compressional stress field (Hinzen 2003;  
106 Dèzes et al. 2004). Those processes can be attributed to the existence of old zones of weakness that  
107 are reactivated under the current stress field (Ahorner 1983; Ziegler and Dèzes 2005; Tesauro et al.  
108 2006). Earthquakes (Fig. 1a) are concentrated in areas that are related to the seismically active  
109 Ochtendunger Fault Zone (Ahorner 1983). These earthquakes are related to stress-field-controlled block  
110 movements, have a weak-to-moderate seismicity, and occur mostly in a shallow crustal depth ( $\leq 15$  km)  
111 with local magnitudes (Richter scale) rarely exceeding 4.0. No fault zones have been reported from our  
112 Goloring study site, and focal depth of earthquakes near the site never exceeded 28 km during our  
113 sampling campaign (BNS 2016).

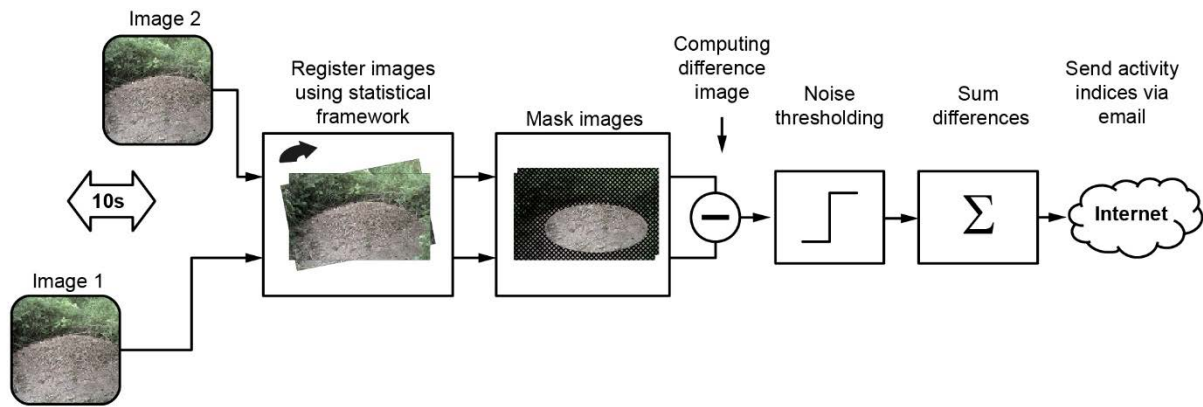


114

115 **Fig. 1** **Location of the Goloring study area (red cross) ≈15 km SE of the Laacher See volcano within**  
116 **the Neuwied Basin (light yellow area). The map (a) shows tectonic structures (black lines) and**  
117 **probability density of the earthquake events from 1977-2016 which are related to the**  
118 **Ochtendunger Fault Zone (rainbow contours). The inset shows the location of study site within**  
119 **Germany. Photographs show (b) the AntCam for continuous monitoring of ant activity and (c)**  
120 **the nest gas probe (all photographs: G. Berberich)**

## 121 **2.2 Monitoring red wood ant activity**

122 Within the research project “GeoBio-Interactions” (March – September, 2016), we monitored RWA  
123 activity using an “AntCam”: a high-resolution camera system (Mobotix MX-M12D-Sec-DNight-  
124 D135N135; 1,280 × 960 pixels) installed ≈5 m from a RWA nest (Fig. 1b). During the 192-hr CH<sub>4</sub>  
125 sampling campaign, which ran from 4–11 August, 2016, ant activities were recorded and time-stamped  
126 continuously (12 Hz). The network-compatible AntCam was connected to a network-attached storage  
127 (NAS) system for data storage via a power-over-Ethernet (POE) supply. A computer connected to the  
128 NAS evaluated the RWA activities on-site and in real time using C++ code to accelerate image  
129 evaluation. Image analysis extended the system of Berberich et al. (2013) and was based on the  
130 difference image technique (Fig. 2). To reduce negative influences caused by, e.g., moving blades of  
131 grass, we used a mask to restrict analysis to only the visible top of the mound. To compensate for slight  
132 movements of the camera, e.g., due to wind, an image registration of the current image relative to the  
133 previous image was done based on mutual information before the determination of the absolute  
134 difference image (Maes et al. 1997). Results of RWA activity were written to a file. Every hour, this file  
135 was sent via email (mobile data transfer, LTE router) to a mail server. Since two different sensors were  
136 used for the day and night, respectively, we computed different polynomials to map the sum of absolute  
137 differences onto manually designed activity categories in a follow-up procedure. The coefficients of the  
138 polynomials were obtained from a minimization of the sum of squared differences between the  
139 polynomial model and the manually assigned category for two selected weeks. A first-order polynomial  
140 was adapted to the daytime data and a third-order polynomial was adapted to the nighttime data. To  
141 avoid numerical difficulties, we first centered and scaled the data by subtracting the mean of the data  
142 during the target time and dividing by the standard deviation. Both values were computed for day- and  
143 nighttime, respectively.



144

145 **Fig. 2 Workflow for acquisition and estimation of RWA activity**

### 146 2.3 Gas sampling and geochemical analyses

147 Field measurements of CH<sub>4</sub> were taken from 4–11 August 2016. A stainless-steel probe (inner diameter  
148 0,6 cm) was inserted into the *F. polycytena* nest to a depth of 80 cm and remained there, unmoved,  
149 during the entire 192-hour sampling campaign. The probe was used for continuous CH<sub>4</sub>/δ<sup>13</sup>C-CH<sub>4</sub>  
150 measurements. The probe was equipped with a flexible tip attached to a pushable rod and a sealable  
151 outlet for docking sampling equipment. The closed probe was inserted into the nest. After opening by  
152 pushing the rod, the probe was evacuated twice, using a 20-ml syringe. After this, the outlet was closed  
153 to prevent atmospheric influence. The outlet was only opened after docking the sampling unit to it.

154 Concentrations of CH<sub>4</sub> and δ<sup>13</sup>C-CH<sub>4</sub> in nest gas (NG) and ambient air (AA) were monitored using a  
155 portable CRDS analyser (G2201-i; Picarro, USA) that measured <sup>12</sup>CH<sub>4</sub>, <sup>13</sup>CH<sub>4</sub> and H<sub>2</sub>O quasi-  
156 simultaneously at 1 Hz, and provided δ<sup>13</sup>C values relative to the Vienna Pee Dee Belemnite standard.  
157 The G2201-i uses built-in pressure and temperature control systems, and automatic water-vapor  
158 correction to ensure high stability of the portable analyzer. Effects of water vapor on the measurement  
159 were corrected automatically by the Picarro® software. The manufacturer guarantees concentration  
160 precision for the analysis of CH<sub>4</sub> in the “high precision mode” of 5 ppbv ± 0.05 % (<sup>12</sup>C) and 1 ppbv ±  
161 0.05% (<sup>13</sup>C) within a concentration range of 1.8–1000 ppm. The guaranteed precision of δ<sup>13</sup>C-CH<sub>4</sub> is  
162 <0.8‰.

163 The CRDS analyzer was deployed in a dry, wind-sheltered location near the RWA nest. Nest gases  
164 were pumped from the aforementioned probe into the CRDS analyzer for analysis of CH<sub>4</sub> and δ<sup>13</sup>C-CH<sub>4</sub>

165 values. Ambient air was measured 2 m away from the nest for 15 min every four hours during the  
166 operation using a 3-way-valve, avoiding disturbance of the nest or the position of the steel probe. All  
167 gases passed through a chemical trap filled Ascarite<sup>®</sup> (sodium hydroxide coated silica;  
168 [www.merckgroup.com](http://www.merckgroup.com)) before entering the system to remove carbon dioxide (CO<sub>2</sub>) because the high  
169 concentrations of CO<sub>2</sub> in the nest samples could interfere with the measurements of CH<sub>4</sub> and δ<sup>13</sup>C-CH<sub>4</sub>.  
170 Gas samples were dried by a Nafion<sup>®</sup> drying tube (Nafion MD110, PermaPure LLC, USA) before  
171 measurements to ensure higher accuracy and subsequently analyzed for CH<sub>4</sub> concentration and δ<sup>13</sup>C-  
172 CH<sub>4</sub>. To assure quality of the CH<sub>4</sub> and δ<sup>13</sup>C-CH<sub>4</sub> values, reference gas measurements were taken every  
173 8 h during the operation. Fluctuations in atmospheric CH<sub>4</sub> and δ<sup>13</sup>C-CH<sub>4</sub> values were validated against  
174 a single, 4-h measurement of ambient air. Carbon isotope ratios are expressed using standard delta (δ)  
175 notation as described by deviations from a standard:  $\delta_{\text{sample}}\text{‰} = ((R_{\text{sample}}/R_{\text{standard}} - 1)) \times 1000$ , where R is  
176 the <sup>13</sup>C/<sup>12</sup>C ratio in the sample or standard. A total of 459 704 samples for both CH<sub>4</sub> and δ<sup>13</sup>C-CH<sub>4</sub> in  
177 nest gas and 27 samples in ambient air were collected and analyzed.

## 178 **2.4 Meteorological Parameters**

179 A radio meteorological station (WH1080) placed 2 m above the ground at the Goloring site continuously  
180 logged meteorological conditions (temperature [°C], humidity [%], air pressure [hPa], wind speed [m/s],  
181 rainfall [mm], and dew point [°C]) at 5-min intervals. The recorded data were downloaded every two  
182 days, checked for completeness, and stored in a data base.

## 183 **2.5 Earthquake events**

184 Data on earthquake events during the sampling campaign were obtained from the seismological  
185 databases provided by the Erdbebenstation Bensberg (BNS, [www.seismo.uni-  
186 koeln.de/events/index.htm](http://www.seismo.uni-koeln.de/events/index.htm)) and by the Landesamt für Geologie und Bergbau, Rheinland-Pfalz (LGB  
187 RLP, <http://www.lgb-rlp.de/fachthemen-des-amtes/landeserdbebendienst-rheinland-pfalz/>). The  
188 probability density of the earthquake events was estimated using the kernel density estimator of Kristan  
189 et al. (2011) using Gaussian kernels.

## 190 **2.6 Earth tides**

191 Cyclic changes in the earth's environment are caused by the gravitational pull of both the Sun and the  
192 Moon on the earth. These result in two slight lunar and two solar tidal bulges ("earth tides"). The two  
193 bulges occur at the surface of the earth that approximately faces the Moon and at the opposite side



194 while the Earth rotates around its axis. Earth tides were calculated using the tool developed by Dehant  
195 et al. and D. Milbert version 15.02.2016 (<http://geodesyworld.github.io/SOFTS/solid.htm>).

## 196 **2.7 Data analysis**

197 All analyses were done using R version 3.3.2 (R Core Team 2016) or MATLAB R2017a.

198 We examined associations between the six measured meteorological variables and RWA activity and  
199 CH<sub>4</sub> concentrations. As many of these variables were correlated with one another, we used principal  
200 components analysis (R function prcomp) on centred and scaled data to create composite “weather”  
201 variables (i.e., principal axes) that were used in subsequent analyses.

202 We used the “median+2MAD” method (Reimann et al. 2005) to separate true peaks in CH<sub>4</sub>  
203 concentrations from background or naturally-elevated concentrations: any observation greater than the  
204 overall median+2MAD (2.31 ppm CH<sub>4</sub> in nest gas and 2.11 ppm CH<sub>4</sub> in ambient air) was considered to  
205 be a peak concentration. Background and elevated CH<sub>4</sub> concentrations were separated based on the  
206 90% quantile of the CH<sub>4</sub> concentration (Phillips et al. 2013). For δ<sup>13</sup>C-CH<sub>4</sub>, we considered concentrations  
207 < -35‰ or > 0‰ to be peak concentrations. Only peaks occurring in both data sets at the same time  
208 were considered to be true peaks. The Keeling plot method (Pataki et al. 2003) was applied to determine  
209 the carbon-isotope composition of the found peaks to obtain insights into the processes that govern the  
210 distinction between isotopes in the ecosystem.

## 211 **3 Results**

### 212 **3.1 Meteorological conditions**

213 During the one-week field campaign in August 2016, air temperatures ranged from 5.7–29.1 °C (mean  
214 = 16.2 °C), with only 2.1 mm rainfall overnight between 9 and 10 August. Variation in atmospheric  
215 pressure (mean 988 ± 2.24 hPa) and wind speed (1.67 ± 1.72 km/h) were small. The first three axes  
216 derived by the principal components analysis accounted for nearly 80% of the variance in the data (Table  
217 1). The first axis represents temperature and humidity, the second axis represents atmospheric pressure  
218 (with additional contributions of humidity and windspeed), and the third axis represents rainfall and  
219 windspeed (with a minor contribution of temperature).

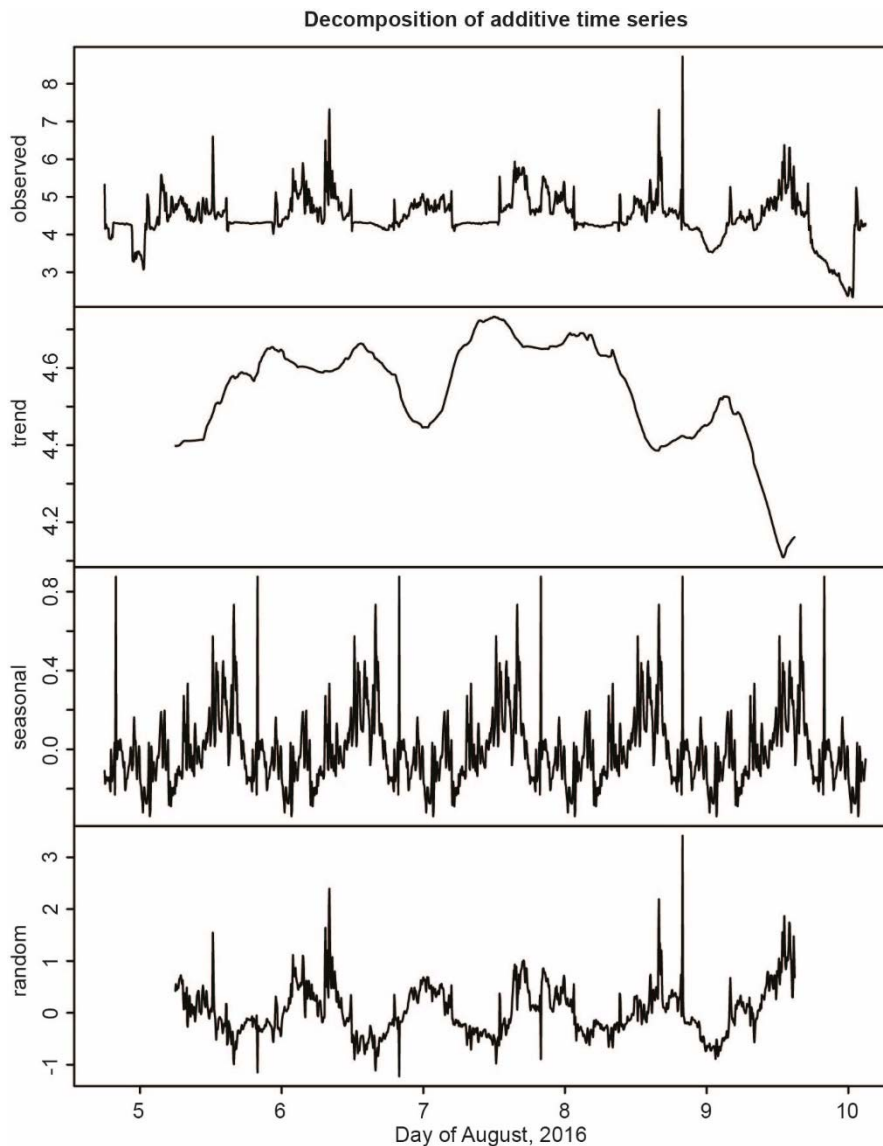
**Table 1 Results of the principal components analysis of the measured weather variables. Values in the first six rows are the loadings of each variable on each of the first three principal axis; only loadings > |0.3| are shown. The last row of the table gives the cumulative proportion of the variance explained by each of the first three principal axes**

<b>Variable</b>	<b>PC-1</b>	<b>PC-2</b>	<b>PC-3</b>
Temperature (°C)	-0.69		0.3
Atmospheric Pressure (hPa)		0.62	
Dew-point (°C)	-0.43	0.49	
Relative humidity (%)	0.48	0.45	
Rainfall (mm)			0.77
Windspeed (km/h)		-0.41	0.50
<b>Cumulative variance explained</b>	0.34	0.59	0.77

220

### 221 **3.2 RWA activity**

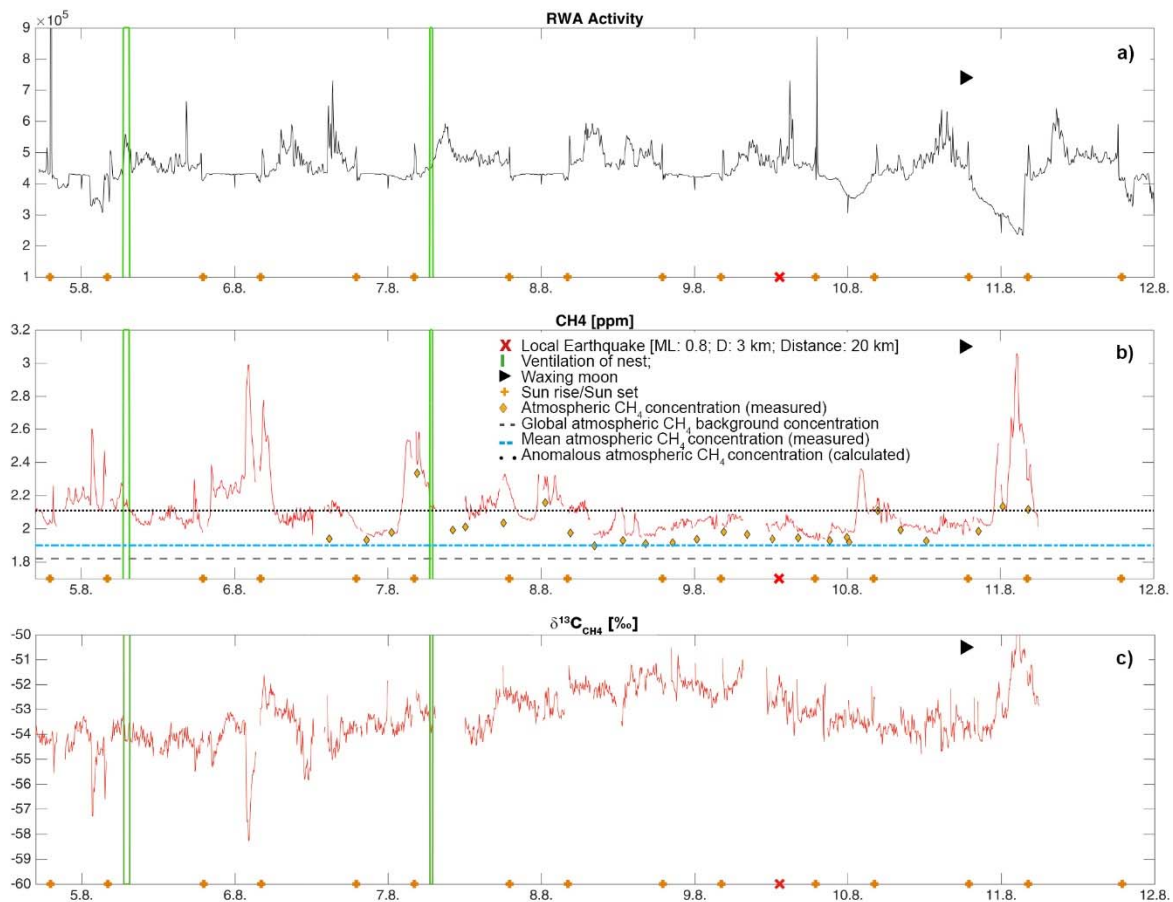
222 Ants were most active during the late afternoon and early evening hours (Fig. 3). The video streams  
223 showed that the ants went on foraging, building and maintaining the nest as they had done since the  
224 start (on March, 18<sup>th</sup>) of our longer 7-month field campaign. Decomposition of the time-series into its  
225 additive components illustrated that during the one-week gas-sampling campaign, there was a trend  
226 towards increasing activity over the first four days, followed by a sharp decline towards the end of the  
227 week (Fig. 3). There were two noticeable peaks of activity, at mid-day and early afternoon, followed by  
228 sharp spikes in activity near 16:30 hours (Fig. 3).



229

230 **Fig. 3 Additive time-series decomposition of median RWA activity. An extreme spike in ant activity**  
231 **(observed = 12 units on 04-August at 19:14 UTC and 25 units on 04-August at 19:19 UTC) are**  
232 **not shown to enhance clarity of the “observed” time-series**

233 No nuptial flight happened during this week. Ventilation phases of the nest took place in the early  
234 morning (6:40 – 7:30 UTC) on 5 August for 50 minutes and on 7 August for 20 minutes (6:40 – 7:00  
235 UTC) after sunrise with varying ant activities (Fig. 4). On two days (07.08. and 09.08.), at 04:30 and  
236 05:50 (UTC), respectively, golden hammer birds (*Emberiza citronella*) were “anting” for  $\approx 5$  min to kill  
237 parasites on their feathers with formic acid; a mouse was observed on the nest at 22:00 (UTC) for 10  
238 minutes on 04.08.16. Only one earthquake occurred nearby (local magnitude: 0.8; depth: 3 km; distance:  
239 20 km). This micro-earthquake neither influenced degassing nor RWA activity.



240

241 **Fig. 4** Time-series plots of median RWA activities (a), CH<sub>4</sub> (b), and  $\delta^{13}\text{C}\text{-CH}_4$  (c) in nest gas, ventilation  
242 phases (green lines) of the nest, sunrise/sunset (orange crosses), and a single local earthquake  
243 (red cross) during the sampling week in August 2016. Reference lines indicate the global  
244 atmospheric CH<sub>4</sub> background concentration (Saunois et al. 2016; black dashed line), the local  
245 mean CH<sub>4</sub> atmospheric concentration (blue dotted line), and the calculated anomalous  
246 atmospheric CH<sub>4</sub> concentration (black dotted line)

247 Median RWA activity and the three principal axes of weather were modestly associated, and accounted  
248 for only 8% of the variance in ant activity (Table 2). The ant activity increased slightly at lower  
249 temperatures (PC-1) and slightly decreased when rainfall (PC-3) was present. PC-2 was not associated  
250 significantly with RWA activity.

**Table 2** Summary ANOVA table of the linear model examining the effects of weather conditions on  
median RWA activity. The estimate is the slope describing the relationship between each  
principal component and median RWA activity. The remaining columns are the degrees of

freedom, mean square, and F-statistic for each term in the model. (\*\* $P < 0.001$ ;  $^{NS}P > 0.5$ ).

Overall model  $r^2 = 0.08$ ;  $F_{3,1536} = 47.57$ ,  $P < 0.001$

	Estimate	Df	MS	F
PC-1	0.19	1	110.8	120.6***
PC-2	-0.01	1	0.3	0.3 <sup>NS</sup>
PC-3	-0.11	1	20.0	21.8***
Residual		1563	0.9	

251

### 252 3.3 CH<sub>4</sub> and δ<sup>13</sup>C-CH<sub>4</sub> in nest gas

253 Concentrations of CH<sub>4</sub> in the nest exceeded the global atmospheric background concentration (1.82  
 254 ppm; Sauniois et al. 2016) and ranged from 1.93 to 3.07 ppm (Fig. 4 and Table 5). δ<sup>13</sup>C-CH<sub>4</sub> ranged  
 255 from -58.48 to -49.54‰ (Fig. 5). Atmospheric CH<sub>4</sub> concentrations were slightly variable (1.90 – 2.33  
 256 ppm). The calculated anomalous threshold concentration for atmospheric CH<sub>4</sub> was 2.11 ppm CH<sub>4</sub>  
 257 (Fig.4). Only four measurements out of 27 exceeded this threshold. Weather conditions explained 22%  
 258 of the variation in δ<sup>13</sup>C-CH<sub>4</sub> (‰), and decreased with all measured weather variables (Table 4).

**Table 3 Summary ANOVA table of the linear model examining the effects of weather conditions on CH<sub>4</sub> concentration (ppm). The estimate is the slope describing the relationship between each principal component and CH<sub>4</sub> concentration. The remaining columns are the degrees of freedom, mean square, and F-statistic for each term in the model. (\*\* $P < 0.001$ ; \* $P < 0.5$ ).**

Overall model  $r^2 = 0.19$ ;  $F_{3,1536} = 121.5$ ,  $P < 0.001$

	Estimate	Df	MS	F
PC-1	-0.3	1	263.1	323.8***
PC-2	0.1	1	29.8	36.6***
PC-3	0.04	1	3.4	4.1*
Residual		1563	0.8	

259

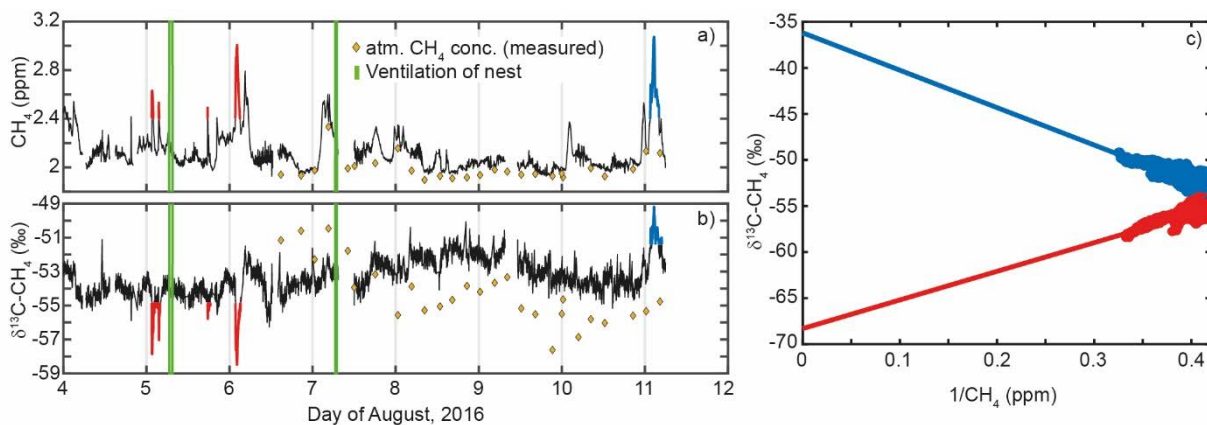
**Table 4 Summary ANOVA table of the linear model examining the effects of weather conditions on δ<sup>13</sup>C-CH<sub>4</sub> (‰). The estimate is the slope describing the relationship between each principal**

component and CH<sub>4</sub> concentration. The remaining columns are the degrees of freedom, mean square, and F-statistic for each term in the model. (\*\*\*)  $P < 0.001$ . Overall model  $r^2 = 0.22$ ;  $F_{3,1536} = 149.5$ ,  $P < 0.001$

	Estimate	Df	MS	F
PC-1	0.22	1	153.2	196.8***
PC-2	-0.24	1	137.8	177.0***
PC-3	-0.19	1	58.2	74.8***
Residual		1563	0.8	

260

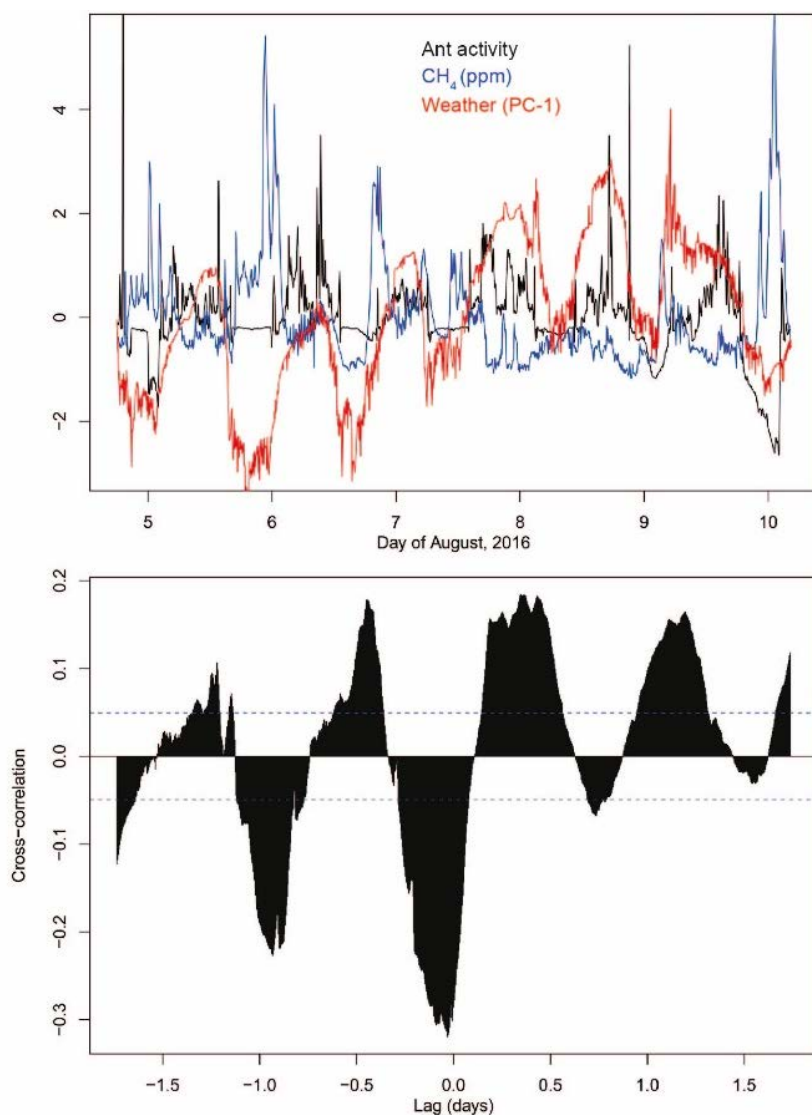
261 Eight significant peaks in nest gas were found for CH<sub>4</sub> and  $\delta^{13}\text{C-CH}_4$  (Fig. 5a, b). These peaks occurred  
 262 between 17:39 (UTC) and 06:54 (UTC) the following day, but were otherwise not temporally predictable.  
 263 Results of the Keeling plots (Pataki et al. 2003) revealed two signatures for  $\delta^{13}\text{C-CH}_4$  at  $-37\text{‰}$  and  
 264  $-69\text{‰}$  in nest gas (Fig. 5c).



265

266 **Fig. 5** Peak concentrations in CH<sub>4</sub> (a) and  $\delta^{13}\text{C-CH}_4$  (b) and Keeling plot of  $\delta^{13}\text{C-CH}_4$  (c) from nest gas.  
 267 Note the peaks indicate two signatures for  $\delta^{13}\text{C-CH}_4$  in nest gas at  $-37\text{‰}$  and  $-69\text{‰}$  (c)

268 Joint visualization of the time series of ant activity, methane concentrations, and weather reveal that all  
 269 the time series exhibited a periodicity of approximately 24 hours. (Fig. 6), and cross-correlations showed  
 270 positive and negative peaks at daily intervals. The absolute value of the cross-correlation coefficient  $\leq$   
 271 0.3, and the strongest cross-correlation occurred at a lag of  $\approx -30$  minutes, less than the original filter  
 272 width of the ant activity time series.

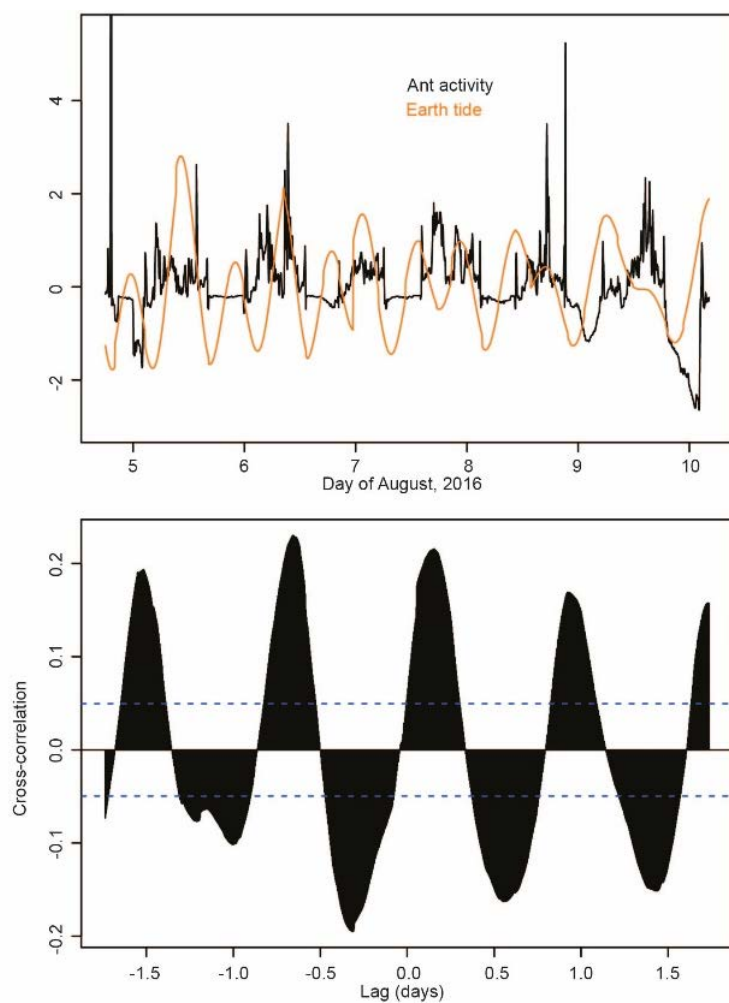


273

274 **Fig. 6** Top: Time-series plot of median ant activity (black), methane concentration (blue), and weather  
275 conditions (PC-1, red). All values are centered and scaled (i.e., are reported in sd units). Bottom:  
276 Cross-correlation between median ant activity and methane activity

### 277 3.4 Earth tides

278 Earth tides were basically semi-diurnal, and we observed a slight increasing trend in amplitude during  
279 the intensive sampling period (Fig. 7, top). The cross-correlation between ant activity and earth tides  
280 never exceeded 0.25 (Fig. 7, bottom). Methane activity (Fig. 8) showed a correlation-coefficient with  
281 earth tides of  $\approx -0.4$  at a lag of 6–8 hours. The cross-correlation between the earth tides and  $\delta^{13}\text{C-CH}_4$   
282 was  $\leq |0.15|$  (Fig. 8, bottom).

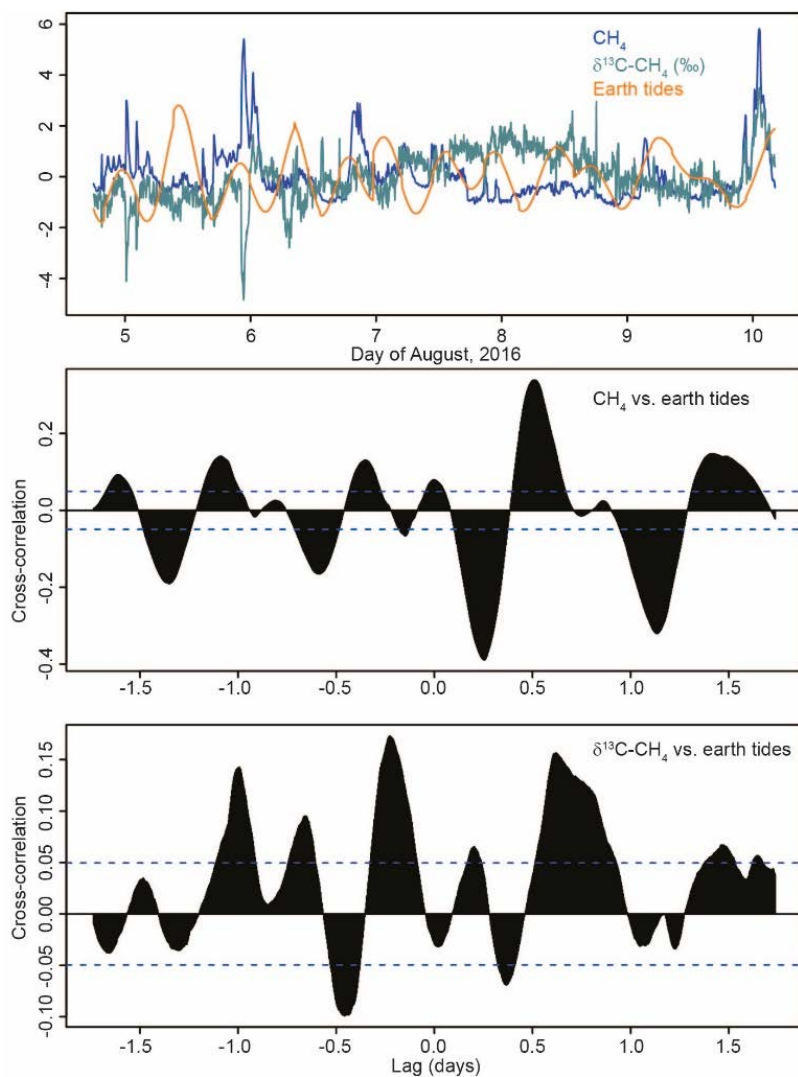


283

284 **Fig. 7** Relationships between ant activity and earth tides. Top: time-series of centered and scaled

285 data. Bottom: cross-correlation of the time-series of ant activity and earth tides





286

287 **Fig. 8** Relationships between CH<sub>4</sub> (blue), δ<sup>13</sup>C-CH<sub>4</sub> (green), and earth tides (orange). Top: time-series of  
288 centered and scaled data. Middle and bottom: cross-correlation of the time-series of CH<sub>4</sub> and  
289 δ<sup>13</sup>C-CH<sub>4</sub> with earth tides

## 290 4 Discussion

### 291 4.1 Meteorological Conditions

292 Meteorological conditions were stable during the sampling week. Variation in atmospheric pressure was  
293 small and there was almost no rainfall. Less than 25% of the variance in CH<sub>4</sub> and δ<sup>13</sup>C-CH<sub>4</sub> were  
294 accounted for by weather conditions (*cf.* Toutain and Baubron 1999).

## 295 **4.2 RWA activities**

296 During the investigation period, ant activity was higher than we had observed in 2009-2012, although  
297 an “M-shaped” pattern in daily activity was still identifiable (Berberich et al. 2013). Relatively high RWA  
298 activities during the late afternoon and early evening hours could be attributable to direct sun hitting the  
299 nest during that time or with activities associated with rebuilding damage to the nest that had occurred  
300 on 18 March. Additional external agents, including mice and “anting” birds, did not influence ant activities  
301 during the sampling week. Ant activity was only weakly correlated with weather (see also Berberich et  
302 al. 2013) or methane seepage.

## 303 **4.2 CH<sub>4</sub> and δ<sup>13</sup>C-CH<sub>4</sub> in nest gas**

304 Measured atmospheric CH<sub>4</sub> concentrations were always lower than CH<sub>4</sub> in RWA nests and there  
305 seemed to be little influence of atmospheric CH<sub>4</sub> on CH<sub>4</sub> in the nests. Rather, elevated CH<sub>4</sub>  
306 concentrations in nest gas appear to result from a combination of microbial activity and transport through  
307 fault networks. Comparison of δ<sup>13</sup>C-CH<sub>4</sub> nest gas signatures with published data suggests that it can be  
308 attributed to two different sources (Fig. 9).

309 The δ<sup>13</sup>C-CH<sub>4</sub> signature of -69‰ in nest gas indicates a microbial source, such as decomposing organic  
310 matter that is high in nutrients (Keppler et al. 2006; Jílková et al. 2016). This result supports the findings  
311 of Jílková et al. (2016) that the aboveground parts of wood ant nests are hot-spots of CH<sub>4</sub> production.

312 The second isotope signature, -37‰ δ<sup>13</sup>C-CH<sub>4</sub>, can be attributed either to thermogenic/fault-related  
313 (Boothroyd et al. 2016) or to abiotic/fault-related CH<sub>4</sub> formation (Etioppe et al. 2016). Boothroyd et al.  
314 (2016) found a δ<sup>13</sup>C-CH<sub>4</sub> signature of -37‰ for fugitive emission of CH<sub>4</sub> via migration along fault zones  
315 in the United Kingdom. Our result of -37‰ δ<sup>13</sup>C-CH<sub>4</sub> is of the same order (Table 5) and can be attributed  
316 to fault-related CH<sub>4</sub> emission moving through the RWA nest.

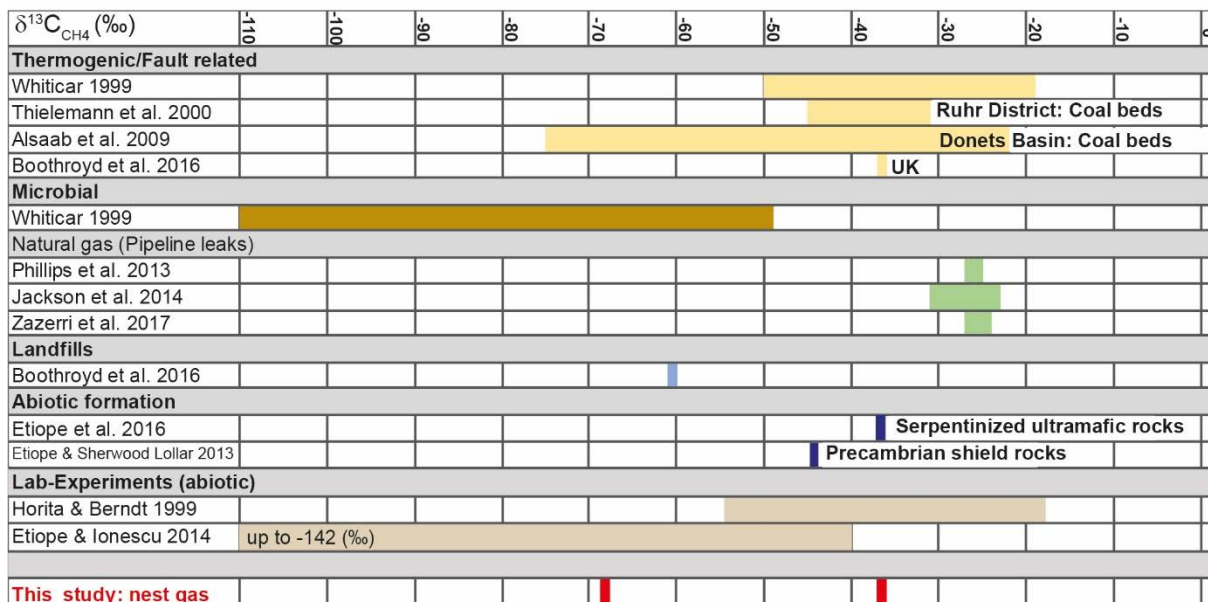
317 Continental loss of volatiles requires tectonically active parts and the formation of fluid-filled conduits  
318 through the continental crust. Suitable locations can be found in extensional regimes and their related  
319 volcanism (Clauser 2002), such as are present in our study area. Gas permeable faults and fractured  
320 rocks are pathways to naturally release significant amounts of “old” CH<sub>4</sub> of crustal origin. Significant  
321 geologic CH<sub>4</sub> emissions, comprising both biogenic and thermogenic CH<sub>4</sub>, are due to hydrocarbon  
322 production in sedimentary basins and, subordinately, to inorganic Fischer-Tropsch type reactions  
323 occurring in geothermal systems (Etioppe and Klusmann 2002). A variety of geological, chemical and

324 biological processes have impacts on the deep carbon cycle. There are three possible sources for the  
 325 fault-related CH<sub>4</sub> we find in RWA nests.

326 **Table 5** Descriptive statistics for nest gas CH<sub>4</sub> (ppm) at Goloring site compared to fugitive emissions of  
 327 CH<sub>4</sub> (ppm) from basin bounding faults in the UK (Boothroyd et al. 2016). SE = 1 standard error of  
 328 the mean

Data amount	Location	Target	N	Mean	SE	Min	Max
All data	Widmerpool	Fault	8313	1.91	0.000395	1.89	2.80
	Lancashire	Fault	5568	1.88	0.00041	1.87	3.18
	Butterknowle	Fault	9283	1.87	0.000342	1.86	3.97
	90 Fathom	Fault landfill	9374	2.24	0.0151	1.86	13.73
	90 Fathom	Fault no landfill	8537	1.89	0.000452	1.86	2.52
	Vale of Eden	Fault	8428	2.20	0.00169	1.87	4.88
<b>This Study</b>	<b>Goloring site</b>	<b>Nest gas</b>	<b>459704</b>	<b>2.13</b>	<b>0.000238</b>	<b>1.93</b>	<b>3.07</b>
Data >90th percentile	Widmerpool	Fault	5	2.34	0.0579	2.24	2.56
	Lancashire	Fault	6	2.56	0.139	2.32	3.18
	Butterknowle	Fault	3	2.34	0.0233	2.29	2.36
	90 Fathom	Fault landfill	692	5.74	0.119	13.73	13.73
	90 Fathom	Fault no landfill	11	2.25	0.0101	2.31	2.31
	Vale of Eden	Fault	2234	2.32	0.00188	2.22	3.23
<b>This Study</b>	<b>Goloring site</b>	<b>Nest gas</b>	<b>47147</b>	<b>2.50</b>	<b>0.00079</b>	<b>2.32</b>	<b>3.07</b>

329



330

331 **Fig. 9** Comparison of δ<sup>13</sup>C-CH<sub>4</sub> in nest gas signatures to published data

332 First, carboniferous coals are sources of thermogenic coalbed methane (CBM) in numerous basins,  
 333 including the Ruhr and Donets Basins. Their δ<sup>13</sup>C are values between -20‰ and -75‰ (Whiticar 1999,

334 Thielemann et al. 2000, Alsaab 2009; Fig. 9). Both basins have coal thicknesses of  $\approx 100$  m  
335 (EnergieAgentur NRW 2009; Alsaab 2009). In our study area, much older Devonian coal seams with  
336 very small thicknesses (LGB RLP 2005) are reported at depths up to 9000 m. Though the study area is  
337 situated in a suitable tectonic compression/extensional regime, any thermogenic  $\text{CH}_4$  would likely be  
338 small because of the very low thickness of the seams and might not even lead to measurable coal-bed  
339  $\text{CH}_4$  concentrations in nest gas. On the other hand, lignite and coal formations are often associated with  
340 aerobic methylophs at depths of over 1 km and are usually considered to be anaerobic (Mills et al.  
341 2010; Stępniewska and Kuźniar 2013; Stępniewska et al. 2014). In the study area, several small lignite  
342 seams (Middle to Upper Eocene) with a thickness of up to 5 m are found in depths of approx. 75 to 160  
343 m. The low thickness and the shallow depth of the lignite may not lead to thermogenic  $\text{CH}_4$  seepage.

344 Second,  $\delta^{13}\text{C}\text{-CH}_4$  in land-based serpentinized ultramafic rocks can be as light as  $-37\text{‰}$ , and methane  
345 from Precambrian shields may exhibit even lower values ( $-45\text{‰}$ ; Etiope and Sherwood Lollar 2013;  
346 Etiope and Schoell 2014; Etiope et al. 2016). Laboratory experiments have produced abiotic methane  
347 with a wide range of  $\delta^{13}\text{C}\text{-CH}_4$  signatures, including isotopically “light” values once thought to be  
348 indicative of biological activity (e.g.  $-19$  to  $-53.6\text{‰}$  by Horita and Berndt 1999;  $-41$  to  $-142\text{‰}$  by Etiope  
349 and Ionescu 2015). Abiotic  $\text{CH}_4$  can be mistaken for biotic  $\text{CH}_4$  of microbial or thermogenic origin  
350 because minor amounts of abiotic gas in biotic gas may prevent its recognition based on C and H isotope  
351 analysis (Etiope et al. 2015; Etiope et al. 2016). Sources of abiotic  $\text{CH}_4$  formation in the study area can  
352 be attributed to magmatic  $\text{CH}_4$  formation due to late magmatic ( $<600^\circ\text{C}$ ) re-distribution of C-O-H fluids  
353 during magma cooling or gas-water-rock-interactions even at low temperatures and pressures (Etiope  
354 and Sherwood Lollar 2013). In the study area, the magmatic source for magmatic  $\text{CH}_4$  formation could  
355 be the so called “Eifel plume”, a region of about 100-120 km in diameter between 50-60 km depth and  
356 at least 410 km depth beneath the study area. The buoyant Eifel plume is characterized by excess  
357 temperature of 100–150 K, has approx. 1% of partial melt and is the main source of regional Quaternary  
358 volcanism (Ritter 2007).

359 Third, gas-water-rock-interactions, including dissolution of C- and Fe-bearing minerals in water at  $\sim 300$   
360  $^\circ\text{C}$  and carbonate methanation between 250 and 800  $^\circ\text{C}$ , do not depend on magma or magma-derived  
361 fluids (Etiope and Scherwood-Lollar 2013; Kietäväinen and Purkamo 2015). The “Klerf Schichten”  
362 (Lower Ems) are alternating layers of reddish Fe-bearing sandstones and C-bearing shales and schists  
363  $\leq 2200\text{-m}$  thick and may be suitable formations for decomposition of C- and Fe-bearing minerals.

364 Paleozoic bedrock sediments, especially the “Sphaerosiderith Schiefer” (Upper Ems; ≤ 150-m thick)  
365 schists with iron concretions (“Eisengallen”), are suitable formations for carbonate methanation: the  
366 decomposition of carbonate minerals (calcite, magnesite, siderite) at lower temperatures in H<sub>2</sub>-rich  
367 environments without mediation of gaseous CO<sub>2</sub> (as it is usually the case for catalytic hydrogenation or  
368 FTT reaction; Etiope and Scherwood-Lollar 2013). Within the habitable zone in the upper crust, at  
369 temperatures >150 °C and in the presence of CO<sub>2</sub>, CO, and H<sub>2</sub>, CH<sub>4</sub> may be produced in aqueous  
370 solution even in the absence of a heterogeneous catalyst or gas phase by a series of redox reactions  
371 leading to the formation of formic acid, formaldehyde and methanol. Finally, abiotic CH<sub>4</sub> also can form  
372 *in situ* through low temperature processes including the Sabatier and Fischer-Tropsch type (FTT)  
373 synthesis reactions with metals like Fe or Ni or clay minerals as catalysts (Etiope and Scherwood-Lollar  
374 2013; Kietäväinen and Purkamo 2015).

375 Because the largest quantities of abiotic gases found on Earth’s surface are produced by low-  
376 temperature gas–water–rock reactions (Etiope et al. 2015) we attribute the –37‰ δ<sup>13</sup>C-CH<sub>4</sub> signature  
377 in RWA nests to fault-related emissions of abiotically formed CH<sub>4</sub> by gas-water-rock reactions occurring  
378 at low-temperatures in a continental setting at shallow depths (micro-seepage). Probable sources might  
379 be Devonian schists (“Sphaerosiderith Schiefer”) with iron concretions (“Eisengallen”) sandstones  
380 and/or the iron-bearing “Klerf Schichten”. However, we cannot exclude the possibility of overlap by  
381 magmatic CH<sub>4</sub> micro-seepage from the Eifel plume.

382 The –37‰ δ<sup>13</sup>C-CH<sub>4</sub> signature in nest gas was detected only once. The micro-earthquake on August 9  
383 did not influence CH<sub>4</sub> degassing because of its far distance (20 km). On August 13, there was another  
384 earthquake (ML: 0.7; D = 13 km) only 2.3 km away from the nest. It might be, that the –37‰ δ<sup>13</sup>C-CH<sub>4</sub>  
385 signature in nest gas was a precursor to the August 13 earthquake, promoting degassing due to an  
386 increase in compressive stress (Boothroyd et al. 2016; Birdsell et al. 2015). But this remains unanswered  
387 as the CH<sub>4</sub> measurement campaign was terminated at August 11.

388 We suggest that future work seek to determine if the –37‰ signature can be attributed to a microbial  
389 source, a purely abiotic source, or a combination of abiotic/thermogenic source. Such a study should  
390 use additional measurements of δ<sup>13</sup>H and run long enough to determine the influence of irregularly timed  
391 earthquake events on patterns of methane degassing.

392

## 393 5 References

- 394 Ahorner L (1983) Historical seismicity and present-day microearthquake activity in the Rhenish Massif,  
395 Central Europe. In: Fuchs K, von Gehlen K, Mälzer H, Murawski H and Semmel A. (eds)  
396 Plateau Uplift. The Rhenish Shield - A Case History. Springer-Verlag, Berlin, pp 198-221
- 397 Alsaab D, Elie M, Izart A, Sachsenhofer RF, Privalov VA, Suarez-Ruiz I, Martinez L, Panova EA  
398 (2009) Distribution of thermogenic methane in Carboniferous coal seams of the Donets  
399 Basin (Ukraine): "Applications to exploitation of methane and forecast of mining hazards".  
400 Int J Coal Geol 78: 27–37
- 401 Berberich G (2010) Identifikation junger gasführender Störungszonen in der West- und Hocheifel mit  
402 Hilfe von Bioindikatoren. Dissertation. University of Duisburg-Essen
- 403 Berberich G, Berberich M, Grumpe A, Wöhler C, Schreiber U (2013) First Results of 2.5 Year  
404 Monitoring of Red Wood Ants' Behavioural Changes and Their Possible Correlation with  
405 Earthquake Events. Animals. doi:10.3390/ani3010063
- 406 Berberich G, Grumpe A, Berberich M, Klimetzek D, Wöhler C (2016) Are red wood ants (*Formica rufa*-  
407 group) tectonic indicators? A statistical approach. Ecol Ind.  
408 doi:10.1016/j.ecolind.2015.10.055
- 409 Berberich G, Schreiber U (2013) GeoBioScience: Red Wood Ants as Bioindicators for Active Tectonic  
410 Fault Systems in the West Eifel (Germany). Animals. doi:10.3390/ani3020475
- 411 Birdsell DT, Rajaram H, Dempsey D, Viswanathan HS (2015) Hydraulic fracturing fluid migration in the  
412 subsurface: a review and expanded modeling results. Water Resour. Res. 51: 7159–7188.
- 413 BNS (2016) Earthquake Data Catalogue. Department of Earthquake Geology of Cologne University.  
414 [www.seismo.uni-koeln.de/catalog/index.htm](http://www.seismo.uni-koeln.de/catalog/index.htm). Accessed 01 September 2016
- 415 Boothroyd IM, Almond S, Worrall F, Davies RJ (2016) Assessing the fugitive emission of CH<sub>4</sub> via  
416 migration along fault zones – Comparing potential shale gas basins to non-shale basins in  
417 the UK. STOTEN. doi.org/10.1016/j.scitotenv.2016.09.052
- 418 Ciotoli G, Lombardi S, Zarlenga F (2006) Natural leakage of helium from Italian sedimentary basins of  
419 the Adriatic structural margin. perspectives for geological sequestration of carbon dioxide.  
420 Advances in the Geological Storage of Carbon Dioxide, 191–202.
- 421 Clauser C, Grieshaber E, Neugebauer HJ (2002) Decoupled thermal and mantle helium anomalies:  
422 Implications for the transport regime in continental rift zones. J Geophys Res.  
423 doi:10.1029/2001JB000675, 2002
- 424 Crockett RGM, Perrier F, Richon P (2010) Spectral-decomposition techniques for the identification of  
425 periodic and anomalous phenomena in radon time-series. Nat Hazards Earth Syst Sci 10:  
426 559–564
- 427 Dehant et al. and Milbert D (2016) Version 15.02.2016  
428 (<http://geodesyworld.github.io/SOFTS/solid.htm>)
- 429 Del Toro I, Berberich GM, Ribbons RR, Berberich MB, Sanders NJ, Ellison AM (2017) Nests of red  
430 wood ants (*Formica rufa*-group) are positively associated with tectonic faults: a double-blind  
431 test. BioRxiv. doi.org/10.1101/113571
- 432 Dèzes P, Schmid SM, Ziegler PA (2004) Evolution of the European Cenozoic Rift System: interaction  
433 of the Alpine and Pyrenean orogens with their foreland lithosphere. Tectonophysics 389:1–  
434 133
- 435 EnergieAgentur NRW (2009) Mine Gas. An energy source in Northrhine-Westphalia. EnergieAgentur  
436 NRW 1/2009
- 437 Etiope G (2009) Natural emissions of methane from geological seepage in Europe. Atmos Environ  
438 43:1430–1443
- 439 Etiope G, Ionescu A (2015) Low-temperature catalytic CO<sub>2</sub> hydrogenation with geological quantities of  
440 ruthenium: a possible abiotic CH<sub>4</sub> source in chromitiferous serpentinitized rocks. Geofluids.  
441 doi:10.1111/gfl.12106

- 442 Etiope G, Judas J, Whiticar MJ (2015) Occurrence of abiotic methane in the eastern United Arab  
443 Emirates ophiolite aquifer. Arab J Geosci. doi:10.1007/s12517-015-1975-4
- 444 Etiope G, Klusman RW (2002) Geologic emissions of methane to the atmosphere. Chemosphere.  
445 49:777-89
- 446 Etiope G, Schoell M (2014) Abiotic gas: atypical, but not rare. Elements – An International Magazine  
447 of Mineralogy, Geochemistry, and Petrology. doi:10.2113/gselements.10.4.291
- 448 Etiope G, Sherwood Lollar B (2013) Abiotic methane on earth. Reviews of Geophysics. doi:  
449 10.1002/rog.20011
- 450 Etiope G, Vadillo I, Whiticar MJ, Marques JM, Carreira PM, Tiago I, Benavente J, Jimenez P, Urresti B  
451 (2016) Abiotic methane seepage in the Ronda peridotite massif, southern Spain. Applied  
452 Geochemistry 66: 101-113
- 453 Hinzen KG (2003) Stress field in the Northern Rhine area, Central Europe, from earthquake fault plane  
454 solutions. Tectonophysics 377: 325–356
- 455 Horita J, Berndt ME (1999) Abiogenic methane formation and isotopic fractionation under  
456 hydrothermal conditions, Science. doi:10.1126/science.285.5430.1055
- 457 Jackson RB, Down A, Phillips NG, Ackley RC, Cook CW, Plata, DL, Zhao KG (2014) Natural gas  
458 pipeline leaks across Washington, DC. Environ. Sci. Technol. 48: 2051–2058
- 459 Jílková V, Pícek T, Šestauberová M, Křišťůfek V, Cajthaml T, Frouz J (2016) Methane and carbon  
460 dioxide flux in the profile of wood ant (*Formica aquilonia*) nests and the surrounding forest  
461 floor during a laboratory incubation. FEMS Microbiol Ecol. doi.org/10.1093/femsec/fiw141
- 462 Keppler F, Boros M, Frankenberg C, Lelieveld J, McLeod A, Pirttilä AM, Röckmann T, Schnitzler JP  
463 (2009) Methane formation in aerobic environments. Env Chem. doi.org/10.1071/EN09137
- 464 Keppler F, Hamilton JTG, Bra M, Röckmann T (2006) Methane emissions from terrestrial plants under  
465 aerobic conditions. Nature. doi:10.1038/nature04420
- 466 Kiätävienen R, Purkamo L (2015) The origin, source, and cycling of methane in deep crystalline rock  
467 biosphere. Front. Microbiol. doi: 10.3389/fmicb.2015.00725
- 468 Kristan M, Leonardis, A, Skočaj, D (2011) Multivariate online kernel density estimation with Gaussian  
469 kernels. Pattern Recognition. doi: 10.1016/j.patcog.2011.03.019
- 470 LGB RLP (2005) Geologie von Rheinland-Pfalz. Schweizbart'sche Verlagsbuchhandlung. Stuttgart
- 471 Litt T, Brauer A, Goslar T, Merk J, Balaga K, Mueller H, Ralska-Jasiewiczowa M, Stebich M, Negendank  
472 JFW (2001) Correlation and synchronisation of Lateglacial continental sequences in northern  
473 Central Europe based on annually laminated lacustrine sediments. In: Björck, S, Lowe, J. J.  
474 and Walker M. J. C. (eds) Integration of Ice Core, Marine and Terrestrial Records of  
475 Termination 1 from the North Atlantic Region. Quaternary Science Reviews 20:1233–1249
- 476 Maes F, Collignon A, Vandermeulen D, Marchal G, Suetens P (1997) Multimodality image registration  
477 by maximization of mutual information. IEEE transactions on medical imaging, 16.2: 187-  
478 198
- 479 Mills C.T, Amano Y, Slater G.F, Dias R.F, Iwatsuki T, Mandernack K.W (2010) Microbial carbon cycling  
480 in oligotrophic regional aquifers near the Tono Uranium Mine, Japan as inferred from d13C  
481 and D14C values of in situ phospholipid fatty acids and carbon sources. Geochim Cosmochim  
482 Acta 74: 3785–3805
- 483 Pataki DE, Ehleringer JR, Flanagan LB, Yakir D, Bowling DR, Still CJ, Buchmann N, Kaplan JO, Berry  
484 JA (2003) The application and interpretation of Keeling plots in terrestrial carbon cycle  
485 research. Global biogeochemical cycles. doi:10.1029/2001GB001850, 2003
- 486 Phillips NG, Ackley R, Crosson ER, Down A, Hutyra LR, Brondfield M, Karr JD, Zhao KG, Jackson RB  
487 (2013) Mapping urban pipeline leaks: methane leaks across Boston. Environ. Pollut. 173:1–  
488 4
- 489 Reimann C, Filzmoser P, Garrett RG (2005) Background and threshold: critical comparison of  
490 methods of determination. Sci. Total Environ. 346: 1– 16.

- 491 Ritter JRR (2007) The Seismic Signature of the Eifel Plume. In: Mantle Plumes - A Multidisciplinary  
492 Approach. Eds: Ritter, Springer-Verlag Berlin Heidelberg, doi: 10.1007/978-3-540-68046-  
493 8\_12
- 494 Ritter JRR, Jordan M, Christensen U, Achauer U (2001) A mantle plume below the Eifel volcanic  
495 fields, Germany. Earth Planet. Sci. Lett, 186: 7–14.
- 496 Sauniois M. et al. (2016) The Global Methane Budget: 2000-2012. Earth Syst. Sci. Data Discuss.  
497 doi:10.5194/essd-2016-25, 2016
- 498 Schoell M (1980) The hydrogen and carbon isotopic composition of methane from natural gases of  
499 various origins. Geochimica et Cosmochimica Acta. doi:10.1016/0016-7037(80)90155-6
- 500 Stępniewska Z, Goraj W, Kuźniar A (2014) Transformation of methane in peatland environments.  
501 Leśne Prace Badawcze (Forest Research Papers). doi:10.2478/frp-2014-0010
- 502 Stępniewska Z., Kuźniar A (2013) Endophytic microorganisms – promising applications in  
503 bioremediation of greenhouse gases. Appl Microbiol Biotechnol. doi:10.1007/s00253-013-  
504 5235-9
- 505 Tesauro M, Hollenstein C, Egli R, Geiger A, Kahle HG (2006) Analysis of central western Europe  
506 deformation using GPS and seismic data. J. Geodynam 42:194-209.
- 507 Thielemann T, Lucke A, Schleser GH, Littke R (2000) Methane exchange between coalbearing basins  
508 and the atmosphere: the Ruhr Basin and the Lower Rhine Embayment, Germany. Org  
509 Geochem 31:1387-1408
- 510 Toutain JP., Baubron JC (1999) Gas geochemistry and seismotectonics: A review. Tectonophysics  
511 304:1-27
- 512 Trinkwasserverordnung in der Fassung der Bekanntmachung vom 10. März 2016 (BGBl. I S. 459), die  
513 durch Artikel 4 Absatz 21 des Gesetzes vom 18. Juli 2016 (BGBl. I S. 1666) geändert  
514 worden ist
- 515 Walker KT, Bokelmann GHR, Klemperer SL, Bock G (2005) Shear-wave splitting around the Eifel  
516 hotspot: Evidence for a mantle upwelling. Geophys J Int 163: 962–980
- 517 Whiticar MJ (1999) Carbon and hydrogen isotope systematics of bacterial formation and oxidation of  
518 methane. Chem Geol 161: 291-314
- 519 Zazzeri G, Lowry D, Fisher RE, France JL, Butler D, Lanoisellé M, Nisbet EG (2017) Identification of  
520 urban gas leaks and evaluation of methane emission inventories using mobile  
521 measurements. Geophysical Research Abstracts. Vol. 19, EGU2017-14409, 2017
- 522 Ziegler P A., Dèzes P (2005) Crustal Evolution of Western and Central Europe. Crust Europe  
523 20.03.05, 31 p.